Observation of isotropic-dipolar to isotropic-Heisenberg crossover in Co- and Ni-substituted manganites

2010 New J. Phys. 12 093039

(http://iopscience.iop.org/1367-2630/12/9/093039)

New Journal of Physics
The open-access journal for physics

Observation of isotropic-dipolar to isotropic-Heisenberg crossover in Co- and Ni-substituted manganites

Yugandhar Bitla[1], S N Kaul[1,5], L Fernández Barquín[2], J Gutiérrez[3], J M Barandiarán[3] and A Peña[4]

[1] School of Physics, University of Hyderabad, Central University PO, Hyderabad-500 046, Andhra Pradesh, India
[2] Dpto. CITIMAC, Universidad de Cantabria, E-39005 Santander, Spain
[3] Dpto. Electricidad y Electrónica, Universidad del País Vasco/EHU, E-39005 Bilbao, Spain
[4] Dpto. de Química Inorgánica, Universidad del País Vasco/EHU, E-39005 Bilbao, Spain
E-mail: kaulsp@uohyd.ernet.in

New Journal of Physics **12** (2010) 093039 (23pp)
Received 13 April 2010
Published 24 September 2010
Online at http://www.njp.org/
doi:10.1088/1367-2630/12/9/093039

Abstract. High-precision ac susceptibility data have been taken on the $La_{0.7}Pb_{0.3}Mn_{1-y}(Co, Ni)_yO_3$ ($y = 0$, 0.1, 0.2 and 0.3) manganite system over a wide range of amplitudes and frequencies of the ac driving field in a temperature range that embraces the critical region near the ferromagnetic (FM)–paramagnetic (PM) phase transition (occurring at the Curie point T_C). Elaborate data analysis was performed that (i) enabled the first observation of a crossover from a three-dimensional (3D; $d = 3$) isotropic long-range dipolar asymptotic critical behavior to a $d = 3$ isotropic short-range Heisenberg critical regime as the temperature is raised from T_C in the compositions $y \neq 0$ (no such crossover is observed in the parent compound, $y = 0$) and (ii) brought out clearly the importance of dipole–dipole interactions between the e_g electron spins and/or between e_g–t_{2g} electron spins in establishing long-range FM order in the insulating state. The final charge and spin states of Co and Ni ions, substituting for the Mn^{3+} and/or Mn^{4+} ions, are arrived at by using a scenario of substitution that is consistent not only with the present results but also with the previously published structural, thermo-gravimetric, bulk magnetization,

[5] Author to whom any correspondance should be addressed.

dc magnetic susceptibility and electrical resistivity data on the same system. The marked similarity seen between the magnetic behavior of the manganite system in question and the quenched random-exchange ferromagnets, within and outside the critical region, suggests that the percolation model forms an adequate description of the FM metal-to-PM insulator transition.

Contents

1. Introduction

The rich diversity and complex nature of the physical phenomena occurring in hole-doped manganite perovskites $R^{3+}_{1-x}A^{2+}_{x}Mn^{3+}_{1-x}Mn^{4+}_{x}O^{2-}_{3}$ (R = La, Sm, Pr, Nd; A = Ca, Sr, Ba, Pb, Cd) have evoked a great deal of interest in the study of such systems (for comprehensive reviews, see [1]–[7]). A quantitative, or in some cases even qualitative, understanding of these physical phenomena necessitated a theoretical approach that goes beyond the double exchange (DE) mechanism, initially proposed for metallic ferromagnetism, in recognizing the importance of (i) the superexchange (SE) between the nearest-neighbor localized t_{2g} spins, which can be antiferromagnetic (AF), or even ferromagnetic (FM), depending on the relevant e_g orbital configurations, (ii) the strong coupling of the twofold degenerate e_g orbitals to the octahedral symmetry-breaking Jahn–Teller (JT) lattice modes and (iii) the strong on-site Mott–Hubbard Coulomb repulsion between two e_g electrons in different orbitals. By contrast, the DE formalism relies on a large Hund coupling between the e_g electron spin and the localized t_{2g} spin on the same site to optimize the kinetic energy, or the inter-site hopping amplitude, of the e_g electrons. However, no single theoretical model is able to adequately handle the interplay between the charge, spin, orbital and lattice degrees of freedom and thereby account for the existence of a variety of phases in the magnetic phase diagram of manganites.

A partial substitution of Mn by TM (TM = Fe, Co, Ni) ions in hole-doped $La_{1-x}A_xMn_{1-y}TM_yO_3$ manganites alters the magnetic and transport properties of the host (LAMO) in a specific fashion, depending on the charge and spin states of the TM solute ions, and thereby provides a fertile testing ground for the theoretical models proposed hitherto. The bulk of such studies have been carried out on the $La_{0.7}Pb_{0.3}Mn_{1-y}(Fe, Co, Ni)_yO_3$ manganite system [8]–[14] rather than on the A = Ca or Sr counterparts [15]–[18]. While there seems to be broad consensus [8, 9, 11], [15]–[18] that the Fe ion exists in the Fe^{3+} high-spin (HS) $t^3_{2g}e^2_g$ $S = 5/2$ state, opinions about the charge and spin states of Co and Ni ions are sharply divided. Configurations such as Co^{3+} low-spin (LS) [11, 13] $t^6_{2g}e^0_g$ $S = 0$, Co^{3+} covalent intermediate-spin (IS) [13, 19, 20] $t^5_{2g}e^1_g$ $S = 1$, Co^{3+} HS [9] $t^4_{2g}e^2_g$ $S = 2$, Co^{4+} HS ([13] and references therein) $t^3_{2g}e^2_g$ $S = 5/2$, Ni^{2+} HS [10] $t^6_{2g}e^2_g$ $S = 1$, Ni^{3+} LS ([14] and references therein) $t^6_{2g}e^1_g$ $S = 1/2$

and Ni^{3+} HS [9] $t_{2g}^5 e_g^2$ $S = 3/2$ have been invoked in the case of Co and Ni ions. In all cases, the solute Fe, Co and Ni ions are supposed to partially substitute for the Mn^{3+} HS $t_{2g}^3 e_g^1$ $S = 2$ ion.

Following the realization that the critical behavior of a spin system in the vicinity of a magnetic order–disorder phase transition is solely governed by the nature of the magnetic ordering present, critical phenomena have been investigated in a large number of manganite systems. However, conflicting reports about the critical exponents that characterize the FM–paramagnetic (PM) phase transition have rendered such studies inconclusive. For instance, the susceptibility critical exponent γ is in the range 1.03–1.45 in $La_{1-x}Ca_xMnO_3$ ($x = 0.2$–0.4) [21]–[25], 1.29–1.41 in $La_{1-x}Ba_xMnO_3$ ($x = 0.27$–0.33) [26]–[28], 1.0–1.38 in $La_{0.67}Sr_{0.33}Mn_{1-y}(Al, Sn, Mo, Ti)_yO_3$ ($y = 0.01$–0.06) [29]–[36], 1.07–1.28 in $La_{1-x}Ba_xMn_{1-y}Sn_yO_3$ ($x = 0.33$–0.4, $y = 0.01, 0.02$) [28, 29], 1.08–1.38 in $La_{1-x}Sr_xMnO_3$ ($x = 0.125$–0.33) [30]–[36] and 1.0–1.456 in $La_{1-x}Pb_xMnO_3$ ($x = 0.1$–0.33) [37]–[39]. Since the reported exponent values either range between the values theoretically predicted for different universality classes (e.g. three-dimensional (3D) isotropic short-range Heisenberg $d = 3, n = 3$ with [40] $\gamma = 1.386(4)$, 3D isotropic short-range Ising $d = 3, n = 1$ with [40] $\gamma = 1.241(2)$, mean-field (MF) with $\gamma = 1.0$, where d and n are the space/lattice dimensionality and spin dimensionality, respectively) or are completely anomalous, the nature of the interactions that sustain FM order below T_C remains obscure. Consequently, the basic issue of whether the percolation picture or the two-fluid model forms a correct description of both the FM–PM and the associated metal–insulator transition cannot be unambiguously resolved.

The unresolved issues mentioned above and the possibility that non-asymptotic data could be responsible for the chaotic dispersion in the γ values prompted us to undertake an exhaustive study of the critical behavior near the FM–PM phase transition in the $La_{0.7}Pb_{0.3}Mn_{1-y}$(Co, Ni)$_yO_3$ ($y = 0, 0.1, 0.2, 0.3$) system. The critical behavior of $y = 0$ (the LPMO host) turns out to be markedly different from that of the Co- and Ni-doped (i.e. $y \neq 0$) samples. Barring a systematic trend with y, the compositions $y = 0.1, 0.2, 0.3$ exhibit essentially the same behavior in the critical region. Therefore, only the representative results (obtained on the compositions $y = 0$ and $y = 0.2$) are presented and the observed trend with y is highlighted as and when required.

2. Experimental details

Extensive ac magnetic susceptibility measurements have been carried out on polycrystalline samples of nominal composition $La_{0.7}Pb_{0.3}Mn_{1-y}$(Co, Ni)$_yO_3$ ($y = 0, 0.1, 0.2, 0.3$) at an ac driving field of rms amplitude ranging from 0.1 to 10 Oe and frequency ranging from 100 Hz to 10 kHz over a wide temperature range $4\,K \leqslant T \leqslant 355\,K$ that embraces the critical region. These samples were prepared by the sol–gel method [8], thoroughly characterized by scanning electron microscopy, energy-dispersive absorption of x-rays and neutron diffraction [13, 14], and are the same as those used previously for bulk magnetization, dc magnetic susceptibility and electrical resistivity measurements [12]–[14]. In the Ni- and Co-containing compounds, the presence of Ni^{2+}, Ni^{3+}, Ni^{4+} and Co^{2+}, Co^{3+}, Co^{4+} at different temperatures [13, 14] was revealed by thermo-gravimetric analysis. The redox titration yielded the Mn^{3+}/Mn^{4+} ratio as 0.35/0.65, 0.28/0.62, 0.20/0.60 and 0.10/0.60 for the compositions y =0, 0.1, 0.2 and 0.3, respectively. Note that the ratio $Mn^{3+}/Mn^{4+} = 0.35/0.65$ in the parent LPMO

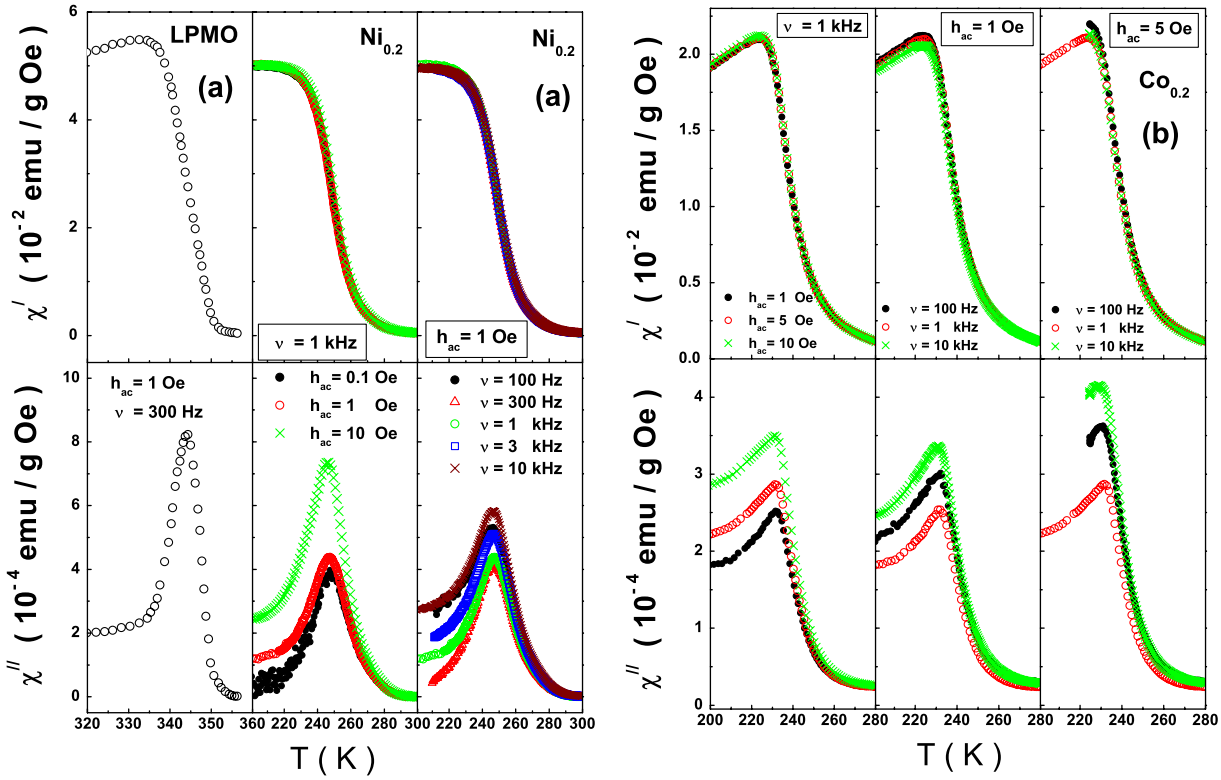

Figure 1. The real, χ', and imaginary, χ'', components of ACS as a function of temperature at a fixed rms field amplitude, $h_{ac} = 1$ Oe, and variable frequency (ν) or at fixed ν and varying h_{ac} for (a) LPMO $\equiv La_{0.7}Pb_{0.3}MnO_3$ and $Ni_{0.2} \equiv La_{0.7}Pb_{0.3}(Mn_{0.8}Ni_{0.2})O_3$ and (b) $Co_{0.2} \equiv La_{0.7}Pb_{0.3}(Mn_{0.8}Co_{0.2})O_3$.

compound differs radically from that (0.70/0.30) expected for the stoichiometric LPMO compound. This departure from the expected Mn^{3+}/Mn^{4+} ratio is caused by the oxygen non-stoichiometry $\delta = 0.17$, which gives rise to vacancies ($\square$) at the cation sites in accordance with the formula $La^{3+}_{[0.7\times3/(3+\delta)]}\square_{[\delta/(3+\delta)]}Pb^{2+}_{[0.3\times3/(3+\delta)]}Mn^{3+}_{[3(0.7-2\delta)/(3+\delta)]}Mn^{4+}_{[3(0.3+2\delta)/(3+\delta)]}\square_{[\delta/(3+\delta)]}O^{2-}_3$. Detailed structural characterization by neutron diffraction confirmed that all the samples are *single phase* and belong to the trigonal space group ($R\bar{3}c$). The Ni or Co substitution causes a slight reduction in the unit-cell volume (average volume change, $\langle \Delta v/v \rangle = 9 \times 10^{-4}$ per at.% Ni and 7.9×10^{-4} per at.% Co) but leaves the remaining structural parameters, such as the tolerance factor, Mn–O bond lengths and Mn–O–Mn, O–Mn–O bond angles, essentially unaltered. The compositions $La_{0.7}Pb_{0.3}MnO_3$, $La_{0.7}Pb_{0.3}Mn_{0.8}Ni_{0.2}O_3$ and $La_{0.7}Pb_{0.3}Mn_{0.8}Co_{0.2}O_3$ are henceforth referred to as LPMO, $Ni_{0.2}$ and $Co_{0.2}$, respectively.

3. Data analysis, results and discussion

Figure 1 displays the temperature dependence of the real (reactive/dispersion), $\chi'(\nu)$, and imaginary (dissipative/absorption), $\chi''(\nu)$, components of ac susceptibility (ACS) for LPMO measured at an ac driving magnetic field of rms amplitude $h_{ac} = 1$ Oe and frequency $\nu = 300$ Hz, and for $Ni_{0.2}$ and $Co_{0.2}$ measured either at a fixed frequency $\nu = 1$ kHz and rms amplitudes $h_{ac} = 0.1, 1, 5, 10$ Oe or at $h_{ac} = 1$ Oe in the frequency range 100 Hz $\leqslant \nu \leqslant$ 10 kHz

over a wide temperature range (which embraces the critical region near the FM–PM phase transition). Recognizing that the critical fluctuations of the order parameter (spontaneous magnetization) have *maximum amplitude* as well as *range* (divergent spin fluctuation–spin fluctuation correlation length) at the critical point, T_C, and that the fluctuations are directly related to dissipation (the fluctuation–dissipation theorem), the temperature T_p at which a sharp peak in $\chi''(T)$ occurs provides a reasonably accurate estimate of T_C. No discernible shift in T_p, or equivalently in the Curie temperature T_C, over a frequency range spanning two decades testifies to a *true thermodynamic* phase transition at T_C. Since χ'' is at least two orders of magnitude smaller (figure 1) than χ' at any temperature, χ' decides the magnitude of ACS. In the PM state ($T \gtrsim T_C$), the inverse *intrinsic* susceptibility, $\chi^{-1}(T)$, varies with temperature as

$$\chi^{-1}(T) = A_{\text{eff}}(T)\epsilon^{\gamma_{\text{eff}}(T)} \quad (\epsilon > 0), \tag{1}$$

where $\epsilon = (T - T_C)/T_C$ and $\gamma_{\text{eff}}(A_{\text{eff}})$ is the effective critical exponent (amplitude). $\chi^{-1}(T)$ is related to the *measured* $\chi'^{-1}(T)$ via the demagnetizing factor, N, as

$$\chi'^{-1}(T) = \chi^{-1}(T) + 4\pi N. \tag{2}$$

According to equation (1), as $T \to T_C$, $\chi^{-1}(T) \to 0$ and $\gamma_{\text{eff}}(T) \to \gamma$ (the asymptotic critical exponent) with the result that $\chi'^{-1}(T) \to 4\pi N$ from equation (2).

The 'range-of-fit' (ROF) analysis (detailed elsewhere [41]–[44]) of the $\chi'^{-1}(T)$ data, based on equations (1) and (2), permits an accurate determination of T_C and N and hence of $A_{\text{eff}}(T)$ and $\gamma_{\text{eff}}(T)$, as elucidated below. Since $T_p \cong T_C$, T_C is *held constant* at *one* of the temperatures ($\approx$80 mK apart), in the range $T_p - 10\,\text{K} \leqslant T_C \leqslant T_p + 10\,\text{K}$, at which χ' has been measured. The parameters N, A_{eff} and γ_{eff} are varied to optimize agreement between the experimentally observed and theoretically predicted (by equations (1) and (2)) $\chi'^{-1}(T)$ over the temperature range $\epsilon_{\min} \leqslant \epsilon \leqslant \epsilon_{\max}$, where $\epsilon_{\min}$ corresponds to the first data point above T_C. In the ROF analysis, the temperature range $\epsilon_{\min} \leqslant \epsilon \leqslant \epsilon_{\max}$ of the fit is varied by keeping $\epsilon_{\min}$ fixed and progressively raising $\epsilon \equiv \epsilon_{\max}$ (by including one more data point above T_C for successive fits), and the variations of N, A_{eff} and γ_{eff} with ϵ are monitored. The correct choice of T_C (and hence of N, A and γ) is the one that yields constant values for N, A_{eff} and γ_{eff} in the asymptotic critical region (ACR), i.e. $N(\epsilon) \to \chi'^{-1}(T_C)/4\pi$, $A_{\text{eff}}(\epsilon) \to A$ and $\gamma_{\text{eff}}(\epsilon) \to \gamma$ as $\epsilon \to 0$. Figure 2 illustrates this behavior of $N(\epsilon)$, $A_{\text{eff}}(\epsilon)$ and $\gamma_{\text{eff}}(\epsilon)$, as an outcome of the ROF analysis, by treating the $\chi'^{-1}(T)$ data taken at $h_{\text{ac}} = 1$ Oe and $\nu = 1$ kHz on $Ni_{0.2}$ as an example. Out of the temperature variations of N, A_{eff} and γ_{eff} yielded by the ROF analysis for the three specified choices of T_C, the criterion that $N(\epsilon)$, $A_{\text{eff}}(\epsilon)$ and $\gamma_{\text{eff}}(\epsilon)$ should attain their limiting but *constant* values as $\epsilon \to 0$ is satisfied only for the (*correct*) choice $T_C = 247.43$ K. The values of T_C determined in this way are displayed in table 1. Figure 3 demonstrates that the value for T_C, so obtained, exactly coincides with the temperature corresponding to the inflection point (where $d\chi'/dT$ goes through a *sharp well-defined minimum*) in the $\chi'(T)$ curve (compare the T_C values given in figures 2 and 3 and table 1) but lies just above (within 1 K) T_p, the temperature at which χ'' peaks. Another important observation is that the T_C of the parent compound gets depressed progressively as the Ni or Co concentration increases but the Co substitution depresses T_C (of the host) at a much faster rate (see also [12]–[14]). The values of T_C, so determined, are in much closer agreement with the numerical estimates directly obtained earlier from the 'zero-field' neutron diffraction data [13, 14] than with those (less reliable values) deduced from the 'in-field' bulk magnetization data through an extrapolation to zero magnetic field.

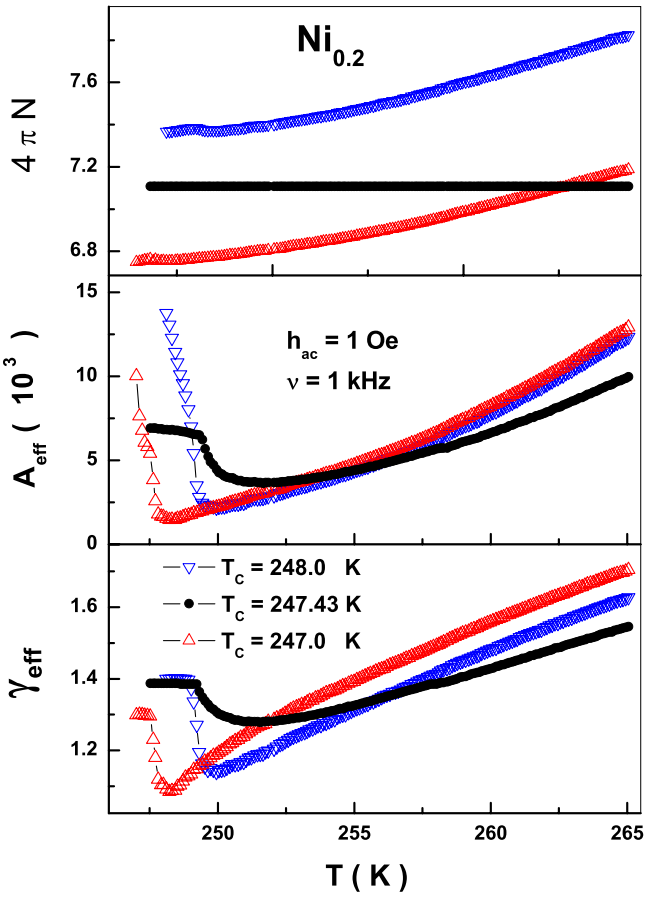

Figure 2. Temperature variations in the parameters $4\pi N$, $A_{\rm eff}$ and $\gamma_{\rm eff}$, yielded by the ROF analysis, corresponding to three different choices of $T_{\rm C}$ (see text for details).

Having determined the $T_{\rm C}$ correctly, the inverse intrinsic susceptibility, $\chi^{-1}(\epsilon)$, is obtained by subtracting $4\pi N(\epsilon = 0)$ from $\chi'^{-1}(\epsilon)$. The behavior of $\chi^{-1}(\epsilon)$ over a wide temperature range above $T_{\rm C}$ is shown in the insets of figure 4. $\chi^{-1}(\epsilon)$, in the critical region, is depicted in the upper panels of figure 4 and compared with the theoretical fits that use the 3D Heisenberg value of $\gamma_{\rm H} = 1.386$ for the asymptotic critical exponent γ in equation (1). The bottom panels display the corresponding percentage deviation of the observed $\chi^{-1}(\epsilon)$ data from the theoretical fits plotted against the reduced temperature ϵ. These deviation plots demonstrate that the 3D Heisenberg value of γ adequately describes $\chi^{-1}(\epsilon)$ in the ACR, more so in the LPMO compound. The physical significance of such deviations, particularly at intermediate temperatures $\epsilon \approx 0.03$ within the critical region, for $Ni_{0.2}$ and $Co_{0.2}$, will become clear at a later stage when a theoretical explanation is provided for the $\gamma_{\rm eff}$ versus ϵ plots shown in figure 5. The salient features of $\gamma_{\rm eff}(\epsilon)$ (figure 5) are as follows. (I) $\gamma_{\rm eff}$ in LPMO assumes the 3D isotropic Heisenberg (1H) value of $\gamma_{\rm H} = 1.386(4)$ at $\epsilon < \epsilon^{\rm H}$ and goes through a peak at $\epsilon_{\rm p} \cong 0.01$ with $\gamma_{\rm eff}^{\rm p} \cong 2.45$ before approaching the MF value of $\gamma = 1$ at $\epsilon > 0.06$. (II) By contrast, *irrespective* of the Co or Ni concentration in the range $0.1 \leqslant y \leqslant 0.3$, a dip in $\gamma_{\rm eff}(\epsilon)$ occurs at $\epsilon_{\rm dip}$, a peak at $\epsilon_{\rm p}$ and $\gamma_{\rm eff}$ attains the values $\gamma_{\rm D} \cong 1.39$, $\gamma_{\rm dip} = 1.280(4)$ and $\gamma_{\rm H} = 1.386(4)$ at $\epsilon \lesssim \epsilon^{*}$, $\epsilon_{\rm dip}$ and ϵ^{**}, respectively. Note that the values of $\epsilon_{\rm dip}$, $\gamma_{\rm dip}$, $\gamma_{\rm H}(\epsilon = \epsilon^{**})$ and ϵ^{**} for different data sets taken on $Co_{0.2}$

Table 1. Critical-point parameters for $Ni_{0.2}$ [$Co_{0.2}$].

	$\nu = 100$ Hz		$\nu = 300$ Hz	$\nu = 1$ kHz				$\nu = 3$ kHz	$\nu = 10$ kHz	
Parameters	$h_{ac} = 1$ Oe	5 Oe	$h_{ac} = 1$ Oe	$h_{ac} = 0.1$ Oe	1 Oe	5 Oe	10 Oe	$h_{ac} = 1$ Oe	$h_{ac} = 1$ Oe	5 Oe
Fit range	4–49		5–64	5–69	4–77		4–65	5–50	5–71	
$\epsilon(10^{-4})$	[4–87]	[7–99]			[5–75]	[5–73]	[5–74]		[3–94]	[6–94]
T_C (K)	247.50(2)		247.42(3)	247.40(3)	247.43(3)		247.49(2)	247.43(2)	247.46(3)	
	[234.40(3)]	[234.45(2)]			[234.35(3)]	[234.38(3)]	[234.45(2)]		[234.40(4)]	[234.40(3)]
γ_D	1.389(2)		1.389(3)	1.389(4)	1.389(3)		1.389(2)	1.389(4)	1.389(2)	
	[1.391(3)]	[1.391(2)]			[1.390(2)]	[1.391(4)]	[1.390(2)]		[1.390(2)]	[1.390(2)]
a_χ	0.090(8)		0.077(2)	0.085(4)	0.077(3)		0.077(2)	0.092(2)	0.080(6)	
	[0.125(6)]	[0.131(6)]			[0.116(8)]	[0.129(7)]	[0.111(5)]		[0.105(2)]	[0.112(4)]
ϵ_{dip}	0.015(3)		0.014(3)	0.014(3)	0.017(3)		0.017(2)	0.016(2)	0.014(3)	
	[0.021(2)]	[0.021(2)]			[0.019(4)]	[0.022(3)]	[0.022(5)]		[0.019(3)]	[0.022(4)]
γ_{dip}	1.282(3)		1.279(3)	1.281(3)	1.280(2)		1.280(2)	1.279(2)	1.283(4)	
	[1.280(3)]	[1.281(5)]			[1.280(5)]	[1.279(2)]	[1.280(2)]		[1.281(2)]	[1.279(2)]
$\gamma_H(\epsilon = \epsilon^{**})$	1.386(3)		1.386(2)	1.386(3)	1.386(2)		1.386(5)	1.386(3)	1.386(5)	
	[1.386(2)]	[1.386(2)]			[1.386(2)]	[1.386(4)]	[1.386(3)]		[1.386(6)]	[1.386(3)]
ϵ^{**}	0.039(2)		0.038(2)	0.041(2)	0.041(2)		0.040(3)	0.039(3)	0.041(2)	
	[0.060(2)]	[0.056(3)]			[0.063(2)]	[0.059(3)]	[0.062(2)]		[0.060(2)]	[0.060(2)]

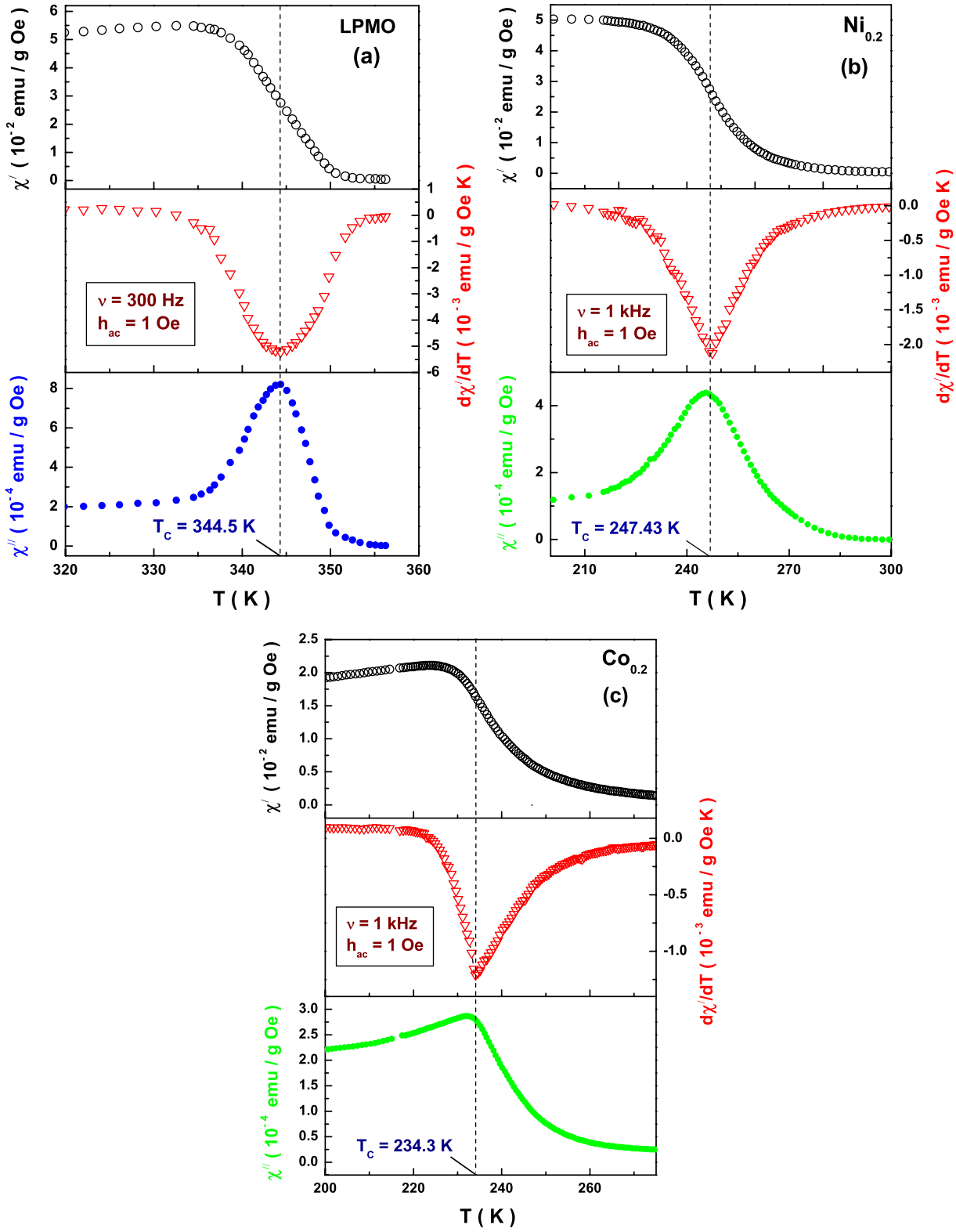

Figure 3. Real part, χ', its temperature derivative, $\mathrm{d}\chi'/\mathrm{d}T$, and imaginary part, χ'', of ACS as functions of temperature for (a) LPMO at $h_{\mathrm{ac}} = 1$ Oe, $\nu = 300$ Hz, (b) $Ni_{0.2}$ at $h_{\mathrm{ac}} = 1$ Oe, $\nu = 1$ kHz, and (c) $Co_{0.2}$ at $h_{\mathrm{ac}} = 1$ Oe, $\nu = 1$ kHz.

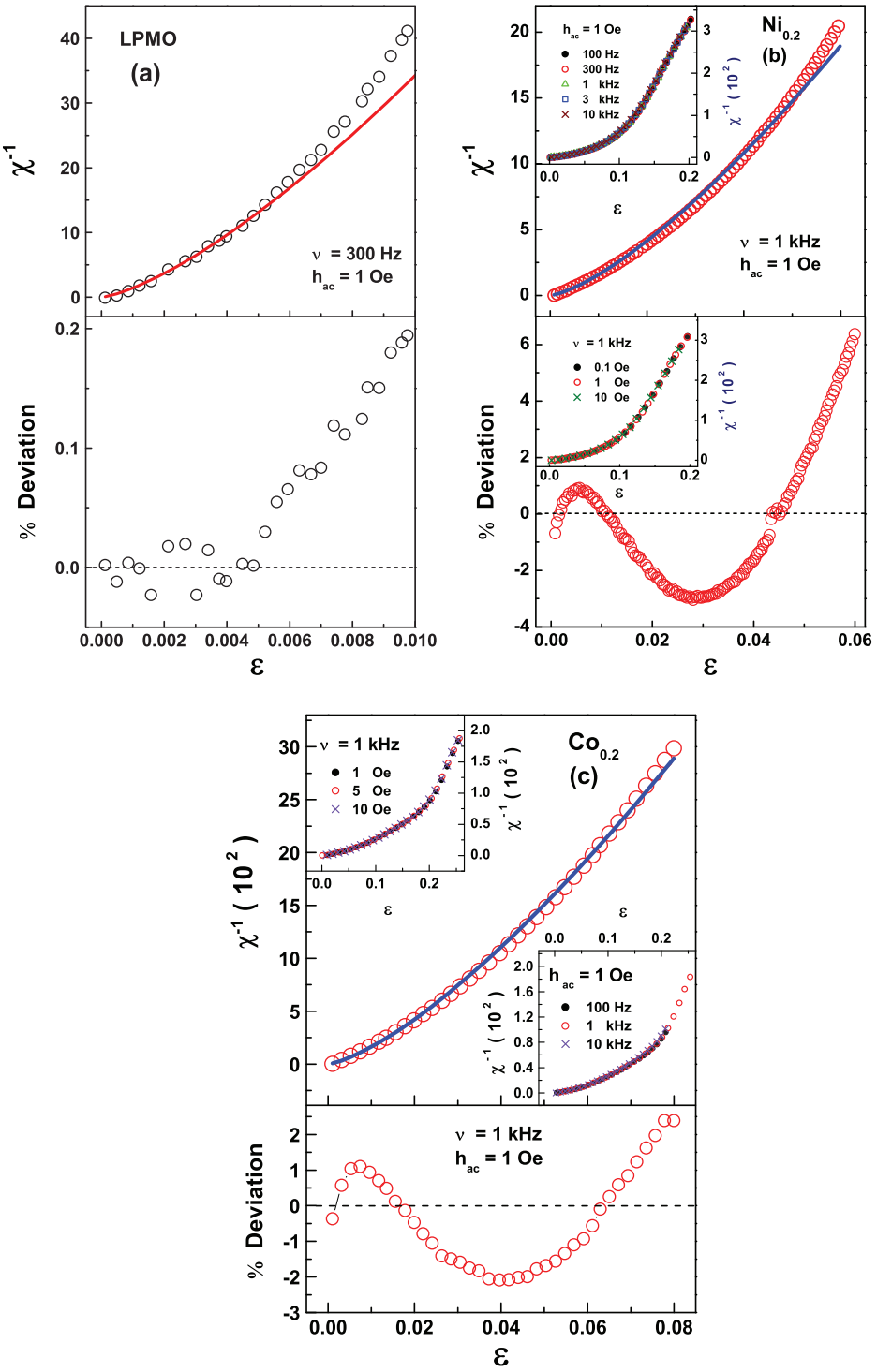

Figure 4. Top panel compares the inverse intrinsic susceptibility, χ^{-1}, as a function of reduced temperature, $\epsilon = (T - T_C)/T_C$, measured (open cicles) in the critical region with the theoretical fit (continuous curve) based on equation (1) of the text with $\gamma = \gamma_{\text{eff}} = 1.386$, while the bottom panel depicts the corresponding percentage deviations of the experimental data from the fit for (a) LPMO, (b) $Ni_{0.2}$ and (c) $Co_{0.2}$. The insets in (b) and (c) show the $\chi^{-1}(\epsilon)$ over a very wide temperature range above T_C.

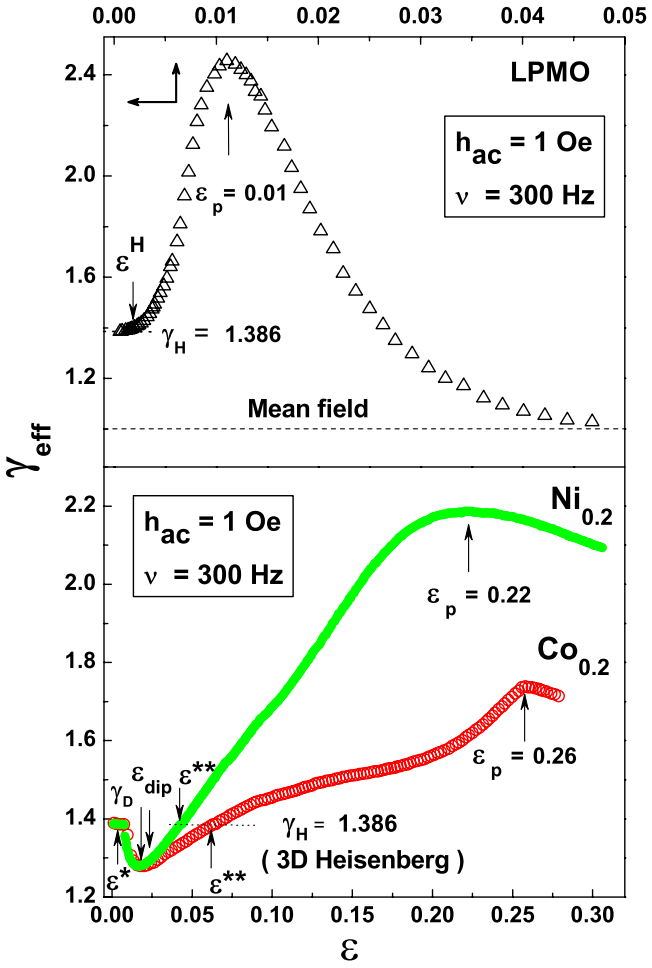

Figure 5. The effective critical exponent for susceptibility, $\gamma_{\rm eff}$, as a function of reduced temperature, $\epsilon = (T - T_{\rm C})/T_{\rm C}$, for LPMO, $Ni_{0.2}$ and $Co_{0.2}$.

and $Ni_{0.2}$ are listed in table 1. (IIIa) As y increases, ϵ^*, $\epsilon_{\rm dip}$, ϵ^{**} and $\epsilon_{\rm p}$ shift to higher temperatures, while the peak value $\gamma_{\rm eff}^{\rm p}$ increases. (IIIb) For a given y, e.g. $Co_{0.2}$ and $Ni_{0.2}$, ϵ^*, $\epsilon_{\rm dip}$, ϵ^{**} and $\epsilon_{\rm p}$ are higher, while $\gamma_{\rm eff}^{\rm p}$ is lower in the case of Co. $\gamma_{\rm eff}(\epsilon)$ of type (I) has been observed [44, 45] previously in several spin systems with quenched random-exchange disorder, which behave as normal ferromagnets down to the lowest temperature. In sharp contrast, $\gamma_{\rm eff}(\epsilon)$ of the type (II) + (III) occurs [44] in amorphous ferromagnets (a-FMs) that have composition close to, but above, the percolation threshold for the appearance of long-range FM order and exhibit re-entrant behavior at low temperatures. Consistent with these observations, the composition $La_{0.7}Pb_{0.3}MnO_3$, corresponding to an Mn^{3+}/Mn^{4+} ratio that maximizes the DE interaction (and hence $T_{\rm C}$), has a collinear FM ground state, whereas in the composition range $0.1 \leqslant y \leqslant 0.3$, the Co- or Ni-substituted LPMO undergoes a transition to the re-entrant-like state (where long-range FM order coexists with cluster spin-glass-like order) at $T \ll T_{\rm C}$ [8]–[14].

In a-FMs, the type (I) $\gamma_{\rm eff}(\epsilon)$ has found the following interpretation in terms of the percolation model [45] in which finite FM clusters coexist with an infinite FM network for $T \leqslant T_{\rm C}$. The spin–spin correlation length, $\xi(T)$, of the $d = 3$ Heisenberg-like FM network diverges at $T = T_{\rm C}$ so that the presence of the spin clusters is not felt in the ACR, $\epsilon \leqslant \epsilon^{\rm H}$, where

the $d = 3$ Heisenberg-like critical behavior is observed. With temperature increasing above T_C, $\xi(T)$ declines rapidly and the infinite FM network breaks up into finite FM clusters, so that at $T > T_C$, finite FM clusters are embedded in a PM matrix. At $\epsilon = \epsilon^H$, $\xi(\epsilon)$ equals the caliper dimension of the largest spin cluster, $(d_c)_{max}$, with the result that the magnetic inhomogeneity in the spin system is now no longer averaged out and γ_{eff} begins to increase as ϵ exceeds ϵ^H till it attains a maximum value γ_{eff}^p at $\epsilon = \epsilon_{max}$ when $\xi(\epsilon) \cong (d_c)_{min}$, the smallest cluster size. It follows that the *smaller* the average cluster size and the *narrower* the cluster size distribution, the *higher* the values of ϵ^H and ϵ_p, the *narrower* the peak in $\gamma_{eff}(\epsilon)$ and the *lower* the peak value γ_{eff}^p (for details, see [45]).

In the case of manganites, *a percolation picture* (strikingly similar to that described above), in which *metallic FM clusters* of various sizes coexist with the *insulating PM matrix* at $T > T_C$, has gained wide acceptance [3, 5] over the years. As the temperature is lowered towards T_C, the localized nearest-neighbor t_{2g} spins (coupled by Heisenberg-like interactions) in the insulating PM phase order better progressively due to the growing spin–spin correlations between them. Ordering of t_{2g} spins, in turn, facilitates hopping of e_g electrons and hence the metallic FM clusters grow in size. For $\epsilon \leqslant \epsilon^H$, $\xi(T)$ is much larger than the size of the largest FM cluster and a $d = 3$ Heisenberg-like critical behavior is expected, as observed in figure 5 for LPMO. However, at $T = T_C$ and for temperatures below T_C, metallic FM clusters coalesce to form an infinite percolating network, in which the finite insulating AF clusters are embedded, and a transition from the insulating ($T > T_C$) to metallic ($T < T_C$) state occurs. Generally, at constant hole density, the transition between the electronic phase-separated metallic FM and insulating AF/CO (charge ordered) phases in manganites is of the *first order*. However, the disorder introduced by a partial but random replacement of R^{3+} ions by A^{2+} ions of larger/smaller ionic radius, and in the present case by the substitution at the Mn site, results in randomly distributed coexisting insulating and metallic percolative clusters. The temperature-induced growth of clusters and the percolation of such clusters render the insulating PM-to-metallic FM transition *continuous* (second order).

Although the mechanisms responsible for the formation of finite FM clusters and FM network/matrix are radically different in the percolation pictures for a-FMs and manganites, the type of interplay between $\xi(T)$ and the temperature-dependent length scale introduced by the finite FM spin clusters at $T > T_C$ [45] permit the conclusion that with respect to the parent compound $y = 0$, the average FM cluster size reduces while the cluster size distribution narrows down as one goes from Ni to Co for a given y. Monte Carlo (MC) simulations [3] on hole-doped manganites have shown that the weaker the disorder, the larger the cluster size. In view of this MC result, the above inference about the cluster size and cluster size distribution asserts that the disorder increases in the sequence LPMO $\rightarrow$ Ni- $\rightarrow$ Co-substituted LPMO.

Figure 6 shows an enlarged view of the steep minimum (dip) in $\gamma_{eff}(\epsilon)$, witnessed in the case of $Ni_{0.2}$ and $Co_{0.2}$ at temperatures close to T_C in figure 5, for the $\chi'(T)$ data taken at $h_{ac} = 1$ Oe for different frequencies (ν) and at $\nu = 1$ kHz for different values of h_{ac}. With a view to bringing out clearly the physical significance of the dip in $\gamma_{eff}(\epsilon)$, and hence of the type (II) + (III) behavior of $\gamma_{eff}(\epsilon)$, a brief account of the relevant theoretical results is given below. Motivated by the fact that long-range dipole–dipole interaction between spins (magnetic dipole moments) is invariably present in all *real* magnetic materials, the renormalization group (RG) calculations [46] on an *isotropic* spin system with $d = 3$ and $n = 3$ revealed that dipolar perturbations render the short-range IH fixed point of RG unstable and give rise to a new *stable* 'isotropic dipolar' (ID) fixed point. However, the critical exponents characterizing

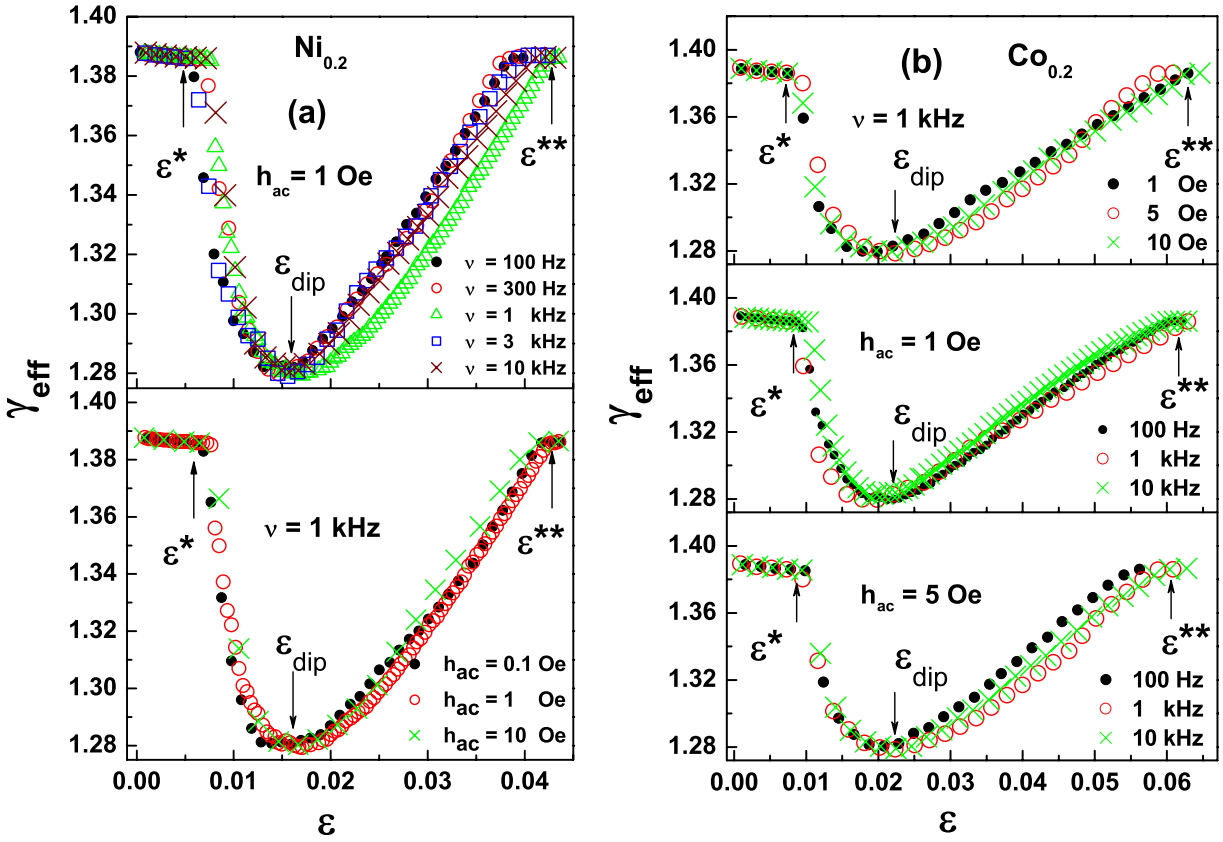

Figure 6. The effective critical exponent for suceptibility, $\gamma_{\rm eff}$, as a function of reduced temperature, $\epsilon = (T - T_{\rm C})/T_{\rm C}$, in the critical regime (which embraces the crossover region) for (a) $Ni_{0.2}$ and (b) $Co_{0.2}$.

the ID fixed point, calculated to two-loop order, are very close [47] to (within 0.5%) those associated with a $d = 3$ pure IH ferromagnet. Subsequent theoretical investigations, using different RG methods [48]–[51], dealt exclusively with the thermally induced crossover from a critical behavior at $T > T_{\rm C}$, governed by the short-range isotropic exchange (Heisenberg) interaction, to the asymptotic ($\epsilon \to 0$) critical behavior dictated by the long-range dipolar interaction. Irrespective of the RG method used, the most remarkable outcome of these theoretical approaches is the occurrence of a deep minimum in $\gamma_{\rm eff}(\epsilon)$ in the crossover region ($\epsilon > 0$), which turns out to be a *universal* feature of the isotropic $d = 3$, $n = 3$ spin systems with *weak* dipolar interactions (compared to the Heisenberg exchange interactions). The numerical results of these RG calculations are summarized in table 2.

The prediction of a dip in $\gamma_{\rm eff}(\epsilon)$ prompted us to attempt a quantitative comparison between the theory and experiment. These RG calculations [48]–[51] yield the final expressions for susceptibility and its effective critical exponent, defined as [52] $\gamma_{\rm eff}(\epsilon) = \partial[\ln \chi^{-1}(\epsilon)]/\partial(\ln \epsilon)$, as

$$\chi(\tau) = \Gamma \tau^{\gamma_{\rm H}/\phi}(1-\tau)^{-\gamma_{\rm D}} p(\tau), \tag{3}$$

$$\gamma_{\rm eff}(\tau) = (1-\tau^{1/\phi})\left[\gamma_{\rm H} + \phi\gamma_{\rm D}\left(\frac{\tau}{1-\tau}\right) + \phi\left(\frac{\tau p'(\tau)}{p(\tau)}\right)\right], \tag{4}$$

Table 2. Theoretically predicted susceptibility critical exponent γ for the isotropic $d = 3$, $n = 3$ spin system with or without long-range dipolar interactions.

RG method	Reference	Isotropic dipolar fixed point (γ_D)	Minimum γ in the crossover region ($\gamma_{\rm dip}$)	Isotropic Heisenberg fixed point ($\gamma_{\rm H}$)	Remarks
$\epsilon(=4-d)$-expansion to $O(\epsilon)$; recursion relations	[46]	1.265		1.25	Quantitatively less accurate estimates
ϵ-expansion to $O(\epsilon^2)$; recursion relations	[47]	1.372		1.365	More refined values
Parquet-graph analysis to $O(\epsilon)$	[48]	1.32	1.24	1.29	Less accurate estimates
Scaling function analysis to $O(\epsilon)$; recursion relations	[49]	1.265	1.21	1.25	Less accurate estimates
Scaling function analysis to $O(\epsilon^2)$; Feynman graph approach	[50]	1.372	1.28(1)	1.365	More refined values; RG calculations to two-loop order.
Field theory; generalized minimal subtraction calculations to $O(\epsilon)$	[51]	1.265	1.22	1.25	Less accurate estimates; RG calculations to one-loop order only.
ϕ^4-field theory; Borel transformation and conformal mapping	[40]			1.386(4)	Most accurate value

where Γ is a non-universal critical amplitude, $\tau = (\epsilon_g/\epsilon_{\rm H})^{\phi}$, $\epsilon_{\rm H} = [T - T_{\rm C}(0)]/T_{\rm C}(0)$, $T_{\rm C}(0) \equiv T_{\rm C}(g = 0)$ is the transition temperature and $\gamma_{\rm H}$ the susceptibility critical exponent of the pure ($g = 0$) IH $d = 3$, $n = 3$ spin system, $\epsilon_g = [T_{\rm C}(g) - T_{\rm C}(0)]/T_{\rm C}(0)$ is the shift in $T_{\rm C}$ caused by ID interactions of relative strength (i.e. the ratio of the ID energy to isotropic exchange energy) g, $\gamma_{\rm D}$ is the susceptibility critical exponent of the $d = 3$ ID fixed point, $\phi = \gamma_{\rm H}$ is the crossover exponent, $p(\tau)$ is the 'correction-to-scaling' function, $\tau^{-1/\phi} - 1 = \widehat{\epsilon} = [(1+\epsilon_g)/\epsilon_g]\epsilon$ and $\epsilon = (T - T_{\rm C}(g))/T_{\rm C}(g)$. The explicit forms of $p(\tau)$ and its derivative with respect to τ, $p'(\tau)$, are given in [50]. Equations (3) and (4) assert the following. (a) The ID interactions become important below a crossover temperature $\epsilon_{\rm co} \approx \epsilon_{\rm dip} \equiv g^{1/\phi}$ such that, for $\epsilon \ll \epsilon_{\rm co}$, the asymptotic critical behavior is that of a $d = 3$ ID ferromagnet, whereas for $\epsilon \gg \epsilon_{\rm co}$ the spin system behaves as a *pure* $d = 3, n = 3$ system. (b) $\gamma_{\rm eff}(\epsilon)$ goes through a minimum in the crossover region such that, at $\epsilon = \epsilon_{\rm dip}$, $\gamma_{\rm eff}$ has the universal (*independent* of the RG coupling parameter [51]) value [50] $\gamma_{\rm dip} = 1.28(1)$, for a weak dipolar system with $g \leqslant 10^{-4}$. (c) $\gamma_{\rm eff} \to \gamma_{\rm D}$ and $\gamma_{\rm H}$ in the ID ($\tau \to 1$) and IH ($\tau \ll 1$) limits. The results for $Ni_{0.2}$ and $Co_{0.2}$, presented in figure 6, testify to the validity of the predictions (a)–(c). Considering that the dipolar interactions between the

localized t_{2g} electron spins are extremely weak compared to the Heisenberg-like SE interactions (which, in turn, are swamped by DE interactions) in hole-doped manganites such as LAMO (A = Ca, Sr, Ba, Pb, Cd), a crossover to the ID critical behavior is expected to occur at temperatures, $\epsilon < \epsilon_{co} \approx 10^{-6}$, which are inaccessible to experiments. Thus, it is not surprising that a dip in $\gamma_{\rm eff}(\epsilon)$ is completely absent in LPMO. In the ACR ($0 < \epsilon \leqslant \epsilon^* \ll \epsilon_{co}$), the expansion of the scaling function $p(\tau)$ in equations (3) and (4) yields the result [42, 53]

$$\chi(\epsilon) = A_\chi \epsilon^{-\gamma_D}[1 + a_\chi\, \epsilon^{\Delta_D}], \tag{5}$$

$$\gamma_{\rm eff}(\epsilon) = \gamma_D - a_\chi \Delta_D \epsilon^{\Delta_D}, \tag{6}$$

$$a_\chi \simeq 0.099 \epsilon_g^{-\Delta_D} \tag{7}$$

and

$$\epsilon_g \cong 0.349\, \dot{\epsilon}, \tag{8}$$

where a_χ and Δ_D are the leading 'correction-to-scaling' amplitude and exponent, and $\dot{\epsilon}$ is the reduced temperature ϵ at which $\chi^{-1} = 4\pi$. The $\gamma_{\rm eff}(\epsilon^{\Delta_D})$ data (symbols) and the best least-squares linear fits (straight lines), based on equation (6), are shown in figure 7 (while the corresponding critical-point parameters are displayed in table 1 for different sets of data taken on $Ni_{0.2}$ and $Co_{0.2}$). It is evident from figure 7 that equation (6) with $\Delta_D = 0.55$ [44] is valid in the ACR ($\epsilon \leqslant \epsilon^*$) and yields the true asymptotic susceptibility critical exponent $\gamma_D = 1.390(1)$, *irrespective* of Co or Ni concentration (and hence γ_D is *universal*, as expected) and (non-universal) *composition-dependent* a_χ. Like a_χ, the width of the ACR *increases with* y and is larger for Co, e.g. $a_\chi = 0.08(1)$, ACR width: $5.0 \times 10^{-4} \leqslant \epsilon \leqslant \epsilon^* = 7.0 \times 10^{-3}$ for $Ni_{0.2}$ and $a_\chi = 0.12(1)$; $5.0 \times 10^{-4} \leqslant \epsilon \leqslant \epsilon^* = 9.0 \times 10^{-3}$ for $Co_{0.2}$ (table 1). This finding implies that among Ni- and Co- doped systems, the dipolar interactions are *stronger* in Co and grow in strength as y increases in both Ni- and Co- containing samples. Inserting the experimental value of $\dot{\epsilon}$ in equations (7) and (8) with $\Delta_D = 0.55$ yields $a_\chi = 0.973(6)$ for $Ni_{0.2}$ and $a_\chi = 0.966(3)$ for $Co_{0.2}$. Compared to the observed values displayed in table 1, these estimates are an order of magnitude higher. In order to make a direct comparison with the predictions of the RG calculations [50], $\gamma_{\rm eff}$ is plotted against $\log_{10}\widehat{\epsilon}$ in figure 8. These $\gamma_{\rm eff}$–$\log_{10}\widehat{\epsilon}$ plots make use of the $\widehat{\epsilon}$ values, estimated from the relation $\widehat{\epsilon} = [(1+\epsilon_g)/\epsilon_g]\epsilon$ and equation (8) using the observed values of $\dot{\epsilon}$. A glance at figure 8 reveals that the theory overestimates the width of the crossover region, underestimates γ_D and γ_H but estimates $\epsilon_{\rm dip}$ with reasonable accuracy and yields the same value $\gamma_{\rm dip} = 1.28$ as observed for $\gamma_{\rm eff}$ at $\epsilon = \epsilon_{\rm dip}$. Considering that the most accurate theoretical value [40] $\gamma_H = 1.386(4)$ is in perfect agreement with the currently determined value of γ_H, more refined RG calculations for the IH–ID crossover are needed to reproduce the experimental values of γ_D and γ_H. That $\epsilon_{\rm dip}$ is higher in Co than in Ni basically reflects that the strength of the dipolar interactions, g, is greater in Co.

A comparison between the deviation plots, shown in the lower panels of figures 4(b) and (c), and the $\gamma_{\rm eff}(\epsilon)$ plots, displayed in figures 6(a) and (b), reveals the following. Firstly, the inferences drawn from a direct fit to the $\chi^{-1}(T)$ data, based on equation (1) and using the 3D Heisenberg value $\gamma_H = 1.386$ for $\gamma_{\rm eff}$, are consistent with the results of the ROF data analysis in that $\gamma_{\rm eff} \cong \gamma_H$ for $\epsilon \leqslant \epsilon^* \simeq 0.01$ and at $\epsilon^{**} \simeq 0.04$ for $Ni_{0.2}$ ($\epsilon^{**} \simeq 0.06$ for $Co_{0.2}$). Secondly, the significantly large deviations of the $\chi^{-1}(T)$ data from the fit, yielded by equation (1) when $\gamma_{\rm eff} = \gamma_H$, at intermediate temperatures (figures 4(b) and (c)) basically reflect the reduced magnitude (figures 6(a) and (b)) of $\gamma_{\rm eff}$, compared to $\gamma_H = 1.386$, in the crossover region.

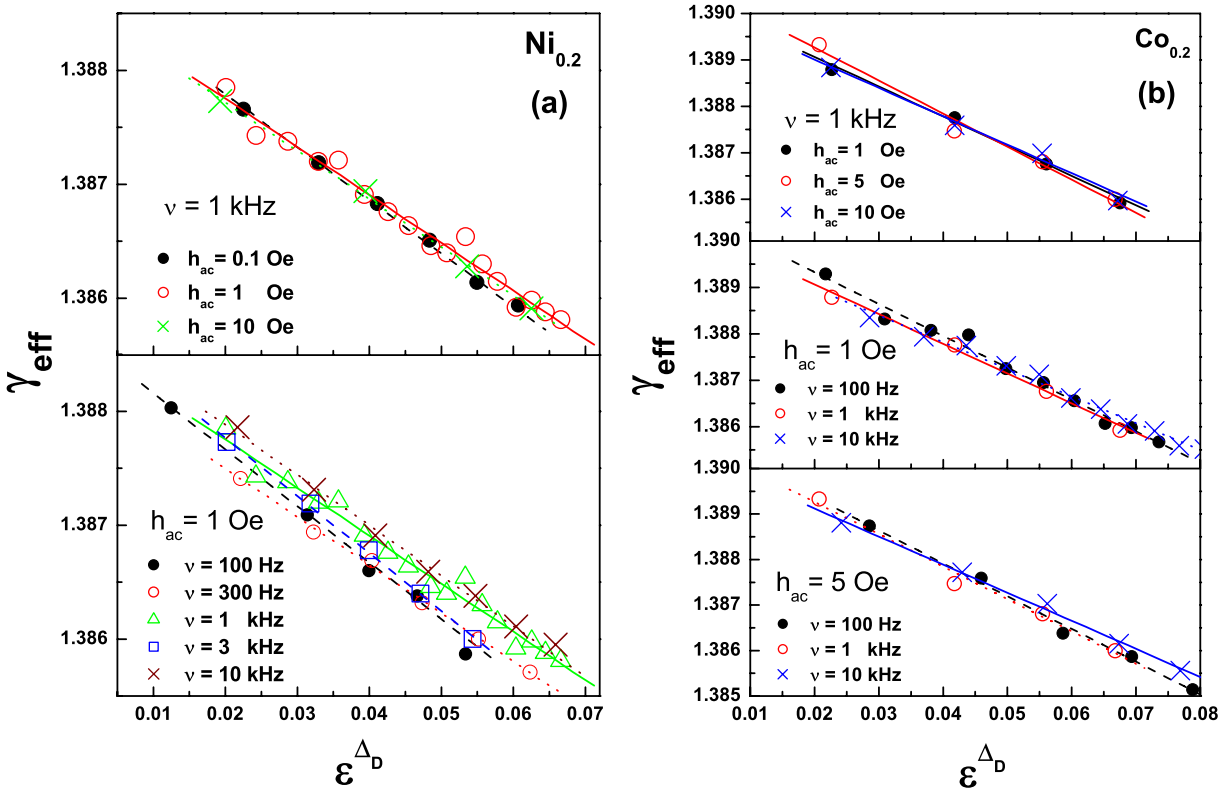

Figure 7. $\gamma_{\rm eff}$ versus $\epsilon^{\Delta_{\rm D}}$ data (symbols) taken in the asymptotic critical region $0 \lesssim \epsilon \leqslant \epsilon^*$ and the linear fits (straight lines through the data points) based on equation (6) for (a) $Ni_{0.2}$ and (b) $Co_{0.2}$.

Thirdly, a wide dispersion in the values of the critical exponent γ reported in the literature for a given series of the hole-doped manganites with or without substitution at the Mn site can be attributed to one or more of the following factors [45]. (a) $T_{\rm C}$ not fixed to an accuracy demanded by a precise determination of the critical exponents. (b) The determinations are based on data that either fall completely within the crossover region or well outside the crossover region or partly overlap the ACR. (c) Uncertainties associated with the extrapolation of the magnetization data, taken in finite magnetic fields, to zero field to arrive at the 'zero-field' quantities, such as spontaneous magnetization and initial susceptibility.

Recognizing that the resolution of the controversy surrounding the charge and spin states of Co and Ni in Co- or Ni-substituted hole-doped manganites is crucial to understanding the origin of dipolar interactions and the process of electron localization/charge ordering, an attempt is made to arrive at the most probable scenario of substitution at Mn^{3+} and/or Mn^{4+} sites that is consistent with the following main observations. (i) Reduction in the unit-cell volume (v)/lattice parameters (a and c), the critical temperature $T_{\rm C}$ and the magnetic moment per 3d transition metal atom (μ) in the FM and PM states, with the Ni or Co concentration, y. (ii) Robustness of the tolerance factor against substitution. (iii) Localization of the conduction electrons as y increases, as inferred from the increase in electrical resistivity with y irrespective of temperature [12]–[14]. The substitution of Mn^{3+} HS ions (with $S = 2$ and ionic radius $r_{\rm ion} = 0.645$ Å) by (a) Ni^{3+} LS ($S = 1/2$, $r_{\rm ion} = 0.56$ Å) or Co^{3+} LS ($S = 0$, $r_{\rm ion} = 0.545$ Å) reduces both v and μ at a rate that is much faster than the observed one; (b) Ni^{2+} HS

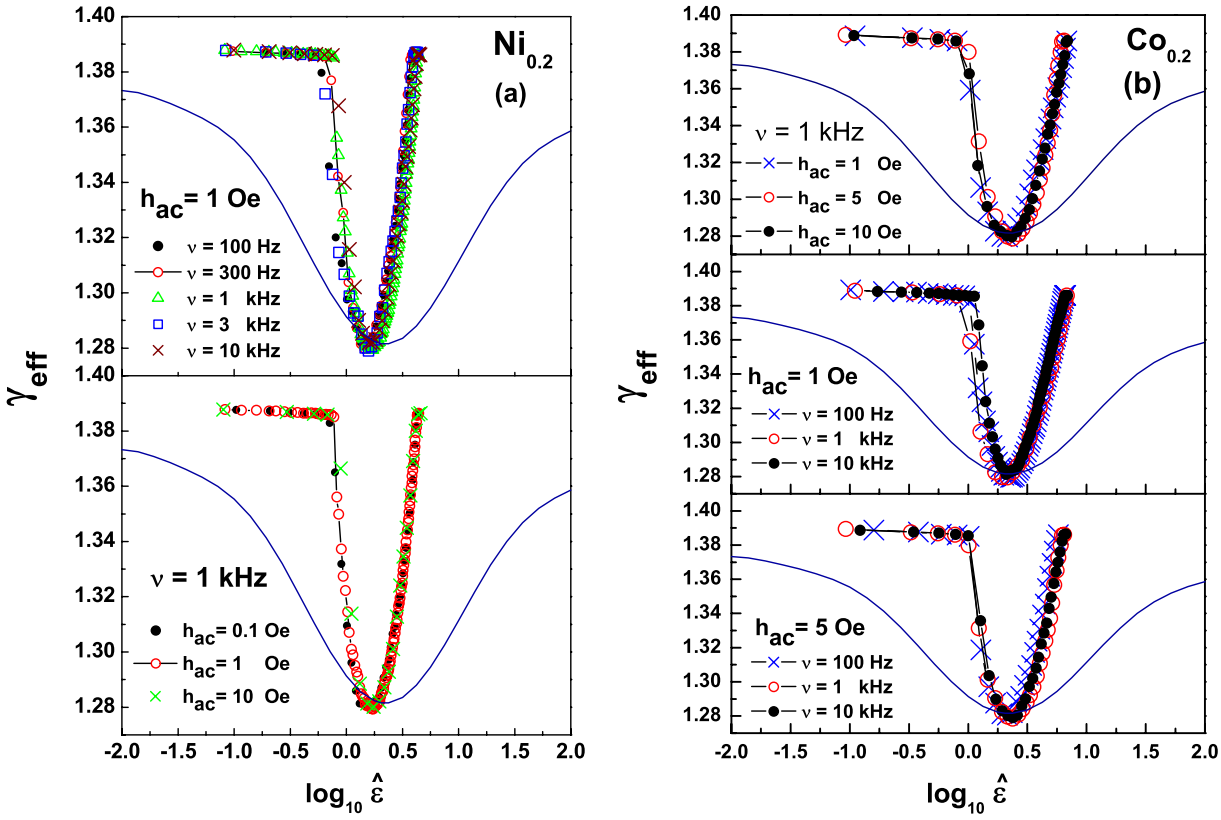

Figure 8. A direct quantitative comparison between theory (solid curve) and experiment (symbols) for (a) $Ni_{0.2}$ and (b) $Co_{0.2}$.

($S = 1$, $r_{ion} = 0.69$ Å) increases v but decreases μ; (c) Co^{3+} HS ($S = 2$, $r_{ion} = 0.61$ Å) reduces v but keeps μ constant; (d) Co^{4+} HS ($S = 5/2$, $r_{ion} = 0.53$ Å) reduces v drastically but increases μ. Thus, the above possibilities (a)–(d) invoked in the literature [9]–[14], [19, 20], are in direct conflict with the consistency conditions (i) and (ii), the latter due to an appreciable change in the tolerance factor. After exhausting other possibilities involving substitution of Mn^{4+} HS ($S = 3/2$, $r_{ion} = 0.53$ Å) by Ni or Co ions of different charge and spin states, we propose the substitution scheme, sketched in figure 9, which is compatible with observations (i)–(iii). In this scheme, Ni^{2+} HS ($t_{2g}^6 e_g^2$, $S = 1$, $r_{ion} = 0.69$ Å) [Co^{2+} LS ($t_{2g}^6 e_g^1$, $S = 1/2$, $r_{ion} = 0.65$ Å)] and Ni^{4+} LS ($t_{2g}^6 e_g^0$, $S = 0$, $r_{ion} = 0.48$ Å) [Co^{4+} HS ($t_{2g}^3 e_g^2$, $S = 5/2$, $r_{ion} = 0.53$ Å)] substitute for Mn^{3+} HS ($t_{2g}^3 e_g^1$, $S = 2$, $r_{ion} = 0.645$ Å) and Mn^{4+} HS ($t_{2g}^3 e_g^0$, $S = 3/2$, $r_{ion} = 0.53$ Å) ions, respectively. Such a substitution introduces the least mismatch between the ionic radii of the solute and the substituted host ions with the result that only a minute reduction in v and essentially no change in the tolerance factor and the bond lengths Mn–O occurs, in accordance with the experimental observation. By virtue of the substitution at the Mn^{3+} and Mn^{4+} sites, Ni^{2+} HS/Co^{2+} LS and Ni^{4+} LS/Co^{4+} HS ions find themselves respectively in the neighborhood of Mn^{4+} and Mn^{3+} ions. In order to minimize the total energy of the system, Ni^{2+} HS and Co^{2+} LS ions assume their stable configurations, Ni^{3+} LS and Co^{3+} HS ions, by donating one e_g electron per ion to Mn^{4+} ions (via the intervening oxygen 2p orbitals) and converting them into Mn^{3+} ions. By contrast, Ni^{4+} LS and Co^{4+} HS ions achieve the same goal (energy minimization) by accepting one e_g electron per ion from the Mn^{3+} HS neighbor (Co^{4+} HS state lowers its

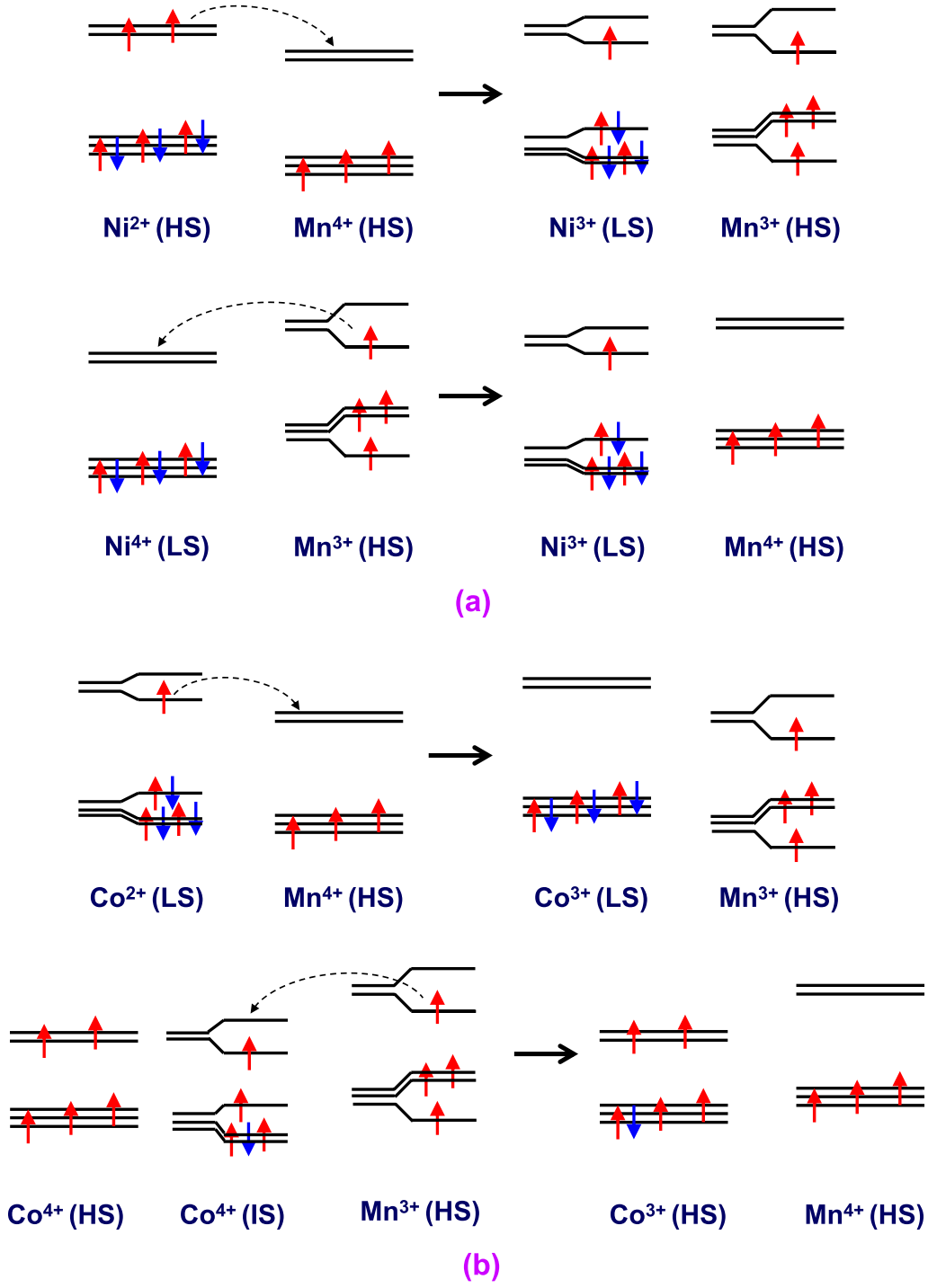

Figure 9. Schematic representation of the charge and spin states of (a) Ni and (b) Co ions in the Ni- and Co-doped LPMO as they evolve from their initial to final configurations through charge transfer.

energy through the JT distortion and changes over to the Co^{4+} IS configuration before accepting the e_g electron) and transform themselves into the stable Ni^{3+} LS and Co^{3+} HS ions (Mn^{3+} HS ions get converted to Mn^{4+} HS ions, in the process), as depicted in figure 9. Since the

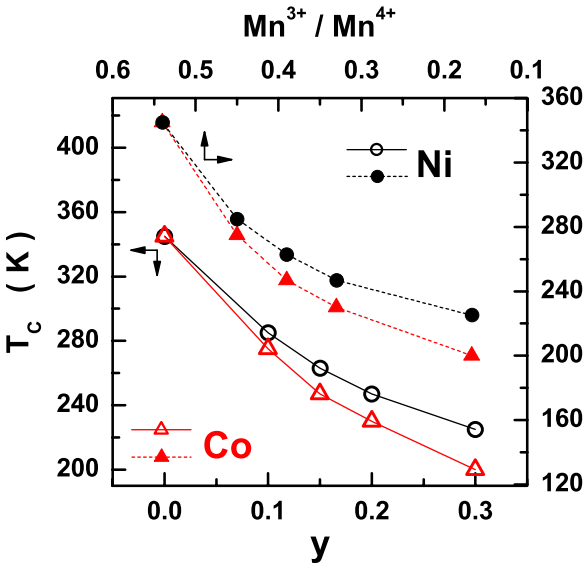

Figure 10. The variation of FM-to-PM transition temperature (T_C) as a function of Co/Ni dopant concentration, y (open symbols), or the Mn^{3+}/Mn^{4+} ratio (filled symbols). The continuous and dashed curves through data points serve as a guide to the eye.

energy considerations do not permit the electron transfer to be reversible, the final configurations Ni^{3+} LS $–O^{2-}–Mn^{3+}$ HS (Ni^{3+} LS–$O^{2-}–Mn^{4+}$ HS) and Co^{3+} LS–$O^{2-}–Mn^{3+}$ HS (Co^{3+} HS–$O^{2-}–Mn^{4+}$ HS) do not revert back to the initial configurations Ni^{2+} HS–$O^{2-}–Mn^{4+}$ HS (Ni^{4+} LS–$O^{2-}–Mn^{3+}$ HS) and Co^{2+} LS–$O^{2-}–$ Mn^{4+} HS (Co^{4+} HS–$O^{2-}–Mn^{3+}$ HS). Consequently, in the final configurations, the e_g and/or t_{2g} electrons on Ni^{3+} LS, Co^{3+} LS/HS, Mn^{3+} HS and Mn^{4+} HS sites become localized and the dipolar interactions couple their spins ferromagnetically. The most remarkable feature of this approach is that one naturally ends up with the most probable charge and spin states for Ni and Co ions as Ni^{3+} LS, Co^{3+} LS and Co^{3+} HS, respectively. In sharp contrast with the Ni- or Co-doped LPMO, in the parent LPMO compound, the DE interactions dominate over the AF $Mn^{3+}–O^{2-}–Mn^{3+}$ and $Mn^{4+}–O^{2-}–$ Mn^{4+} SE interactions and the localization mechanism, brought about by the Ni or Co substitution, is absent and hence the ID interactions do not show up.

Within the framework of the above picture (figure 9), the Co^{3+} HS ion has two localized e_g electrons as against one per Ni^{3+} LS ion. It immediately follows that the Co-substitution should be *more effective* in weakening DE (and hence in reducing T_C), as corroborated by experiments (figure 10). Had the role of such e_g-electron localization been merely to reduce the DE, T_C would have dropped in proportion to the Ni/Co concentration or Mn^{3+}/Mn^{4+} ratio (with a faster drop in the Co case); SE interactions, favoring AF coupling between the t_{2g} electron spins of the ion pairs $Ni^{3+}/Co^{3+}–O^{2-}–Ni^{3+}/Co^{3+}$ or $Mn^{3+}/Mn^{4+}–O^{2-}–Mn^{3+}/Mn^{4+}$, would make the decline of T_C with increasing Ni/Co concentration (or decreasing Mn^{3+}/Mn^{4+} ratio) even faster. As noted from figure 10, this expectation is in direct conflict with the observed slowing down of the rate of decrease of T_C in both cases as the concentration of Ni/Co solute ions increases or the Mn^{3+}/Mn^{4+} ratio decreases. We propose that the *dipolar interactions*, which couple the $e_g–e_g$ ($e_g–t_{2g}$) spins on the Ni^{3+} LS–$O^{2-}–Ni^{3+}$ LS, Ni^{3+} LS–$O^{2-}–Mn^{3+}$ HS, Co^{3+} HS–$O^{2-}–Co^{3+}$ HS (Ni^{3+} LS–$O^{2-}–Mn^{4+}$ HS, Co^{3+} HS–$O^{2-}–Mn^{4+}$ HS) nearest-neighbor ion

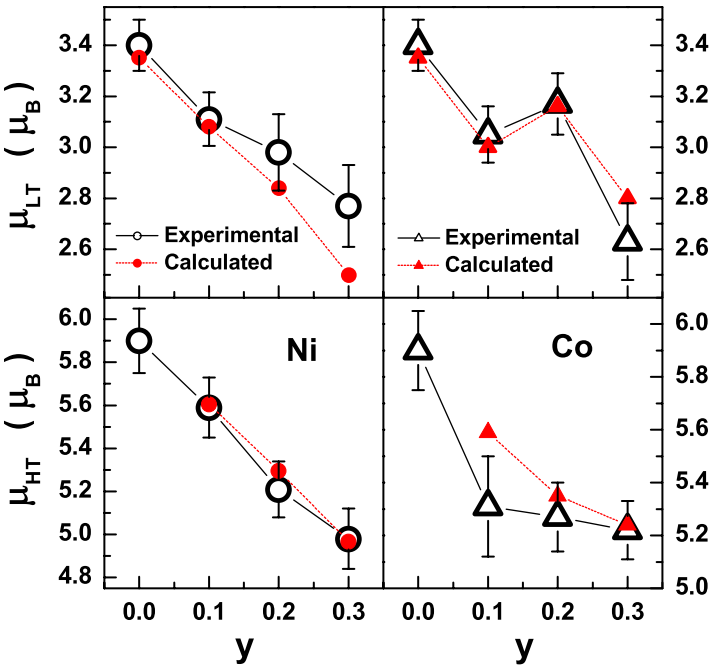

Figure 11. Comparison of the calculated low- and high-temperature magnetic moments with those obtained experimentally for both Ni- and Co-doped LPMO. The continuous and dotted lines joining the data points or the calculated values are a guide to the eye.

pairs ferromagnetically, slow down the rate of decline of T_C caused by the reduced DE and/or enhanced SE. This is so because the dipolar interactions, although *extremely weak* compared to the DE and SE interactions, tilt the balance in favor of FM order when the *competing* DE–FM interactions between e_g electron spins and SE–AF interactions between t_{2g} electron spins are both *large* but of *similar magnitude*. The dipolar interactions are stronger in Co-substituted LPMO because of the greater number of localized e_g electrons and larger magnetic moments on the Co^{3+} HS ion, and this also explains the higher electrical resistivity [12]–[14] for the Co-containing manganites. Assuming that the substitution of Mn^{3+} HS and Mn^{4+} HS ions by Ni or Co solute ions is completely biased by the 35/65::Mn^{3+}/Mn^{4+} ratio prevalent in the LPMO host, we arrive at the values for the low-temperature (saturation) magnetic moment, μ_{LT}, and high-temperature (in the PM state) magnetic moment, μ_{HT}, for all of the compositions in the Ni- and Co-substituted series that are in very good agreement (figure 11) with the corresponding experimental values [13, 14]. In the case of Co-substituted LPMO, the agreement between the calculated and observed values of μ_{LT} and μ_{HT} can be improved further by considering that at low (high) temperatures, almost all of the Co^{3+} ions are in the LS (HS) state, as the energy difference between the two spin states is as low as [54] $\approx$0.03 eV.

Before assessing the impact of the present findings on the current understanding of the underlying physics of the novel physical phenomena exhibited by manganites, the salient features of this work are summarized below. (A) In the optimally hole-doped parent LPMO compound, the SE–AF interactions between the localized t_{2g} electron spins are *completely dominated* by the DE–FM interactions between e_g electron spins and the dipolar interactions between the localized t_{2g} electron spins are *extremely weak* compared to the SE interactions.

Thus, dipolar interactions have essentially no role to play in establishing the FM state in LPMO. (B) Strong evidence for the presence of *finite metallic* FM clusters within the *insulating* PM matrix for $T > T_C$, and hence for the phase separation, is provided by the peak in $\gamma_{eff}(\epsilon)$ at ϵ_p in the parent LPMO compound as well as in the Ni- or Co-substituted LPMO. (C) In LPMO and weakly Ni- or Co-doped ($y < 0.1$) LPMO, finite metallic FM clusters grow in size as the temperature is decreased towards T_C, so much so that at $T \lesssim T_C$, metallic FM clusters coalesce to form an *infinite* FMM percolating network in which *finite* AF *insulating* clusters are embedded, and thus a percolative transition from the insulating ($T > T_C$) to metallic ($T < T_C$) state occurs. (D) As more and more of the Mn ions in LPMO are replaced by Ni or Co ions (i.e. as y increases), an increased number of e_g electrons become localized via the mechanism illustrated in figure 9. Consequently, the DE–FM interactions are rapidly suppressed and become similar in magnitude to the SE–AF interactions, so that even *weak dipolar interactions* between the localized e_g electron spins and/or between e_g–t_{2g} electron spins are able to establish the FM insulating (FI) phase, which grows at the expense of the FMM phase with increasing y. Thus, a transition from the PI phase ($T > T_C$) to the FI phase ($T < T_C$) occurs at $T = T_C$ when the Ni or Co solute concentration exceeds a certain threshold value ($y > 0.2$ in the present case). That the dipolar interactions play a decisive role in establishing FM order in the vicinity of T_C when the fraction of localized e_g electrons becomes substantial ($y \geqslant 0.2$) is clearly borne out by the increase in the ID-to-IH crossover temperature with y. Since the currently studied manganite system has the same underlying physics as other optimally doped manganites, e.g. $La_{0.7}A_{0.3}Mn_{1-y}TM_yO_3$ where A = Ca, Sr, Ba, Cd and TM = Fe, Co, Ni, the above observations (A)–(D) should be applicable to these systems as well and provide a means of resolving the controversy surrounding the nature of the FM–PM phase transition as well as the spin and charge states of Co and Ni in $La_{0.7}A_{0.3}Mn_{1-y}TM_yO_3$ manganites.

In recent years, substantial progress in understanding the pronounced 'electron–hole asymmetry' and the occurrence of a variety of phases in the phase diagram of $La_{1-x}A_xMnO_3$ manganites has been made by recognizing the importance of the competition between DE interactions, Hund coupling between e_g electron spin and localized t_{2g} electron spin, JT electron–phonon coupling between e_g electrons and the local distortions of the MnO_6 octahedron, Coulomb interactions among the e_g electrons and AF Heisenberg coupling between nearest-neighbor t_{2g} spins. However, many aspects of the physics of manganites are still poorly understood. For instance, no general consensus on how the FI state at low doping levels $x \approx 1/8$ evolves from the AF insulating state at $x = 0$ has emerged so far. Taking cognizance of the inference (D), we suggest that the dipole–dipole interaction (completely ignored in the previous considerations) between the *localized e_g electron spins* (regardless of the actual localization mechanism) may hold the key to the formation of the FI phase at low doping levels, as elucidated below. As the hole concentration (x) increases from zero, the DE interaction grows at the expense of the SE interaction so that at a certain value of x, the DE FM interactions between mobile e_g electron spins, become similar in magnitude to, and compete with, the SE AF interactions between localized t_{2g} electron spins, with the result that even extremely weak dipolar interactions suffice to tilt the balance in favour of FM order.

4. Summary and conclusion

An extensive investigation of the magnetic behavior of the $La_{0.7}Pb_{0.3}Mn_{1-y}(Co, Ni)_yO_3$ ($y = 0, 0.1, 0.2, 0.3$) hole-doped manganite system over a wide range of temperatures, which covers

the critical region near the FM–PM phase transition and the PM region, has been carried out by measuring ACS at the ac driving field whose rms amplitudes (frequencies) ranged from 0.1 to 10 Oe (from 100 Hz to 10 kHz). A detailed ROF analysis of the ACS data enabled a precise determination of the Curie temperature, T_C, and hence of the effective critical exponent, γ_{eff}, for susceptibility as a function of reduced temperature, $\epsilon = (T - T_C)/T_C$. The main observations are as follows. In the parent LPMO compound, (I) $\gamma_{eff}(\epsilon) \to \gamma_H = 1.386$ (the 3D IH value) in the ACR and goes through a peak before approaching the MF value of $\gamma = 1$ at $T \gg T_C$. (II) By contrast, regardless of the Ni or Co concentration in the range $0.1 \leqslant y \leqslant 0.3$, as the temperature is raised from T_C, γ_{eff} starts with the value $\gamma_D = 1.390(1)$ in the ACR ($\epsilon \lesssim \epsilon^*$), goes through a steep minimum (dip) at ϵ_{dip} with $\gamma_{dip}(\epsilon = \epsilon_{dip}) = 1.280(4)$, rises to the value $\gamma_H = 1.386(4)$ at ϵ^{**} and then peaks at ϵ_p assuming a value $\gamma_{eff}(\epsilon = \epsilon_p)$, which depends on y. (III) As y increases, ϵ^*, ϵ_{dip}, ϵ^{**} and ϵ_p shift to higher temperatures, while γ_{eff}^p increases. (IV) For a given y, ϵ^*, ϵ_{dip}, ϵ^{**} and ϵ_p are higher, while γ_{eff}^p is lower in the case of Co. (V) A progressive drop in T_C (from its value in the LPMO host) occurs as the Ni or Co concentration increases but the Co-substitution depresses T_C at a much faster rate. However, the rate of decline of T_C slows down with increasing y, i.e. $T_C(y)$ is concave upwards. The RG calculations predict that (a) a 3D isotropic spin system, in which short-range Heisenberg interactions coexist with *weak* long-range dipolar interactions, exhibits a thermally induced crossover from the 3D IH critical behavior to the 3D ID asymptotic critical behavior when the temperature is lowered towards T_C from high temperatures, and (b) the *characteristic feature* of this IH to ID crossover is a dip in $\gamma_{eff}(\epsilon)$ in the crossover region with γ_{eff} attaining the values γ_D in the ACR, $\gamma_{dip} = 1.28(1)$ at ϵ_{dip} and γ_H at ϵ^{**}, respectively. In view of these RG predictions, the observations (II)–(IV) permit us to conclude that an ID-to-IH crossover occurs in the Ni- and Co-substituted LPMO, and the ID interactions, not discernable in the parent LPMO compound, grow in strength with y and, among Ni and Co solutes, are stronger in the Co-substituted LPMO.

Within the framework of a percolation model, the peak in $\gamma_{eff}(\epsilon)$ at ϵ_p in the LPMO host and the Ni- or Co-substituted LPMO is shown to result from an interplay between the diverging spin–spin correlation length of the *insulating* PM matrix as $\epsilon \to 0$ and the temperature-dependent length scale due to the *finite metallic* FM clusters, while the observed upward shift in ϵ_p and the decrease in γ_{eff}^p as one follows the sequence $y = 0 \to$ Ni $\to$ Co (for a given Ni or Co concentration, e.g. $y = 0.2$ in figure 5) imply that the average FM cluster size decreases and the cluster size distribution narrows down. The peak in γ_{eff} for $\epsilon > 0$ thus constitutes a new experimental signature for the phenomenon of phase separation in hole-doped manganites. To address the issues connected with the localization of e_g electrons (and hence weakening of DE) and the origin of dipolar interactions, we have proposed the charge and spin states for Ni and Co ions in the Ni- and Co-substituted LPMO that are consistent not only with the present results but also with the previously published structural (neutron diffraction), thermo-gravimetric, bulk magnetization, dc magnetic susceptibility and electrical resistivity data on the same system. Finally, the physical implications of our results, so far as the physics of manganites is concerned, are discussed in the preceding section.

Acknowledgments

YB thanks the Council for Scientific and Industrial Research (CSIR), India, for support of this work through a Junior Research Fellowship and the Centre for Nanotechnology (funded by the

Department of Science and Technology, New Delhi) for permission to use the Quantum Design Physical Property Measurement System (PPMS).

References

[1] Coey J M D, Viret M and von Molnar S 1999 *Adv. Phys.* **48** 167
[2] Salamon M B and Jaime M 2001 *Rev. Mod. Phys.* **73** 583
[3] Dagotto E, Hotta T and Moreo A 2001 *Phys. Rep.* **344** 1
[4] Goodenough J B 2004 *Rep. Prog. Phys.* **67** 1915
[5] Dagotto E 2005 *New J. Phys.* **7** 67
[6] Tokura Y 2006 *Rep. Prog. Phys.* **69** 797
[7] Ramakrishnan T V 2007 *J. Phys.: Condens. Matter* **19** 125211
[8] Gutiérrez J, Barandiarán J M, Peña A, Lezama L, Insausti M, Rojo T and Pizarro J L 2000 *J. Phys.: Condens. Matter* **12** 10523
Gutiérrez J, Peña A, Barandiarán J M, Pizarro J L, Hernandez T, Lezama L, Insausti M and Rojo T 2000 *Phys. Rev.* B **61** 9028
[9] Young S L, Chen Y C, Horng L, Wu T C, Chen H Z and Shi J B 2000 *J. Magn. Magn. Mater.* **289** 145
Young S L, Chen Y C, Chen H Z, Horng L and Hsueh J F 2002 *J. Appl. Phys.* **91** 8915
[10] Pal S, Bose E, Chaudhuri B K, Yang H D, Neeleshwar S and Chen Y Y 2005 *J. Magn. Magn. Mater.* **293** 872
[11] Gritzner G, Koppe M, Kellner K, Przewoznik J, Chmist J, Kolodziejczyk A and Krop K 2005 *Appl. Phys.* A **81** 1491
Gritzner G, Koppe M, Kellner K, Przewoznik J, Chmist J, Kolodziejczyk A and Krop K 2008 *Appl. Phys.* A **90** 359
[12] Peña A, Gutiérrez J, Barandiarán J M, Pizarro J L, Rojo T, Lezama L and Insausti M 2001 *J. Magn. Magn. Mater.* **226–230** 831
Peña A, Gutiérrez J, Barandiarán J M and Rojo T 2004 *J. Magn. Magn. Mater.* **272–276** e1425
[13] Peña A, Gutiérrez J, Gil de Muro I, Campo J, Barandiarán J M and Rojo T 2006 *Eur. J. Inorg. Chem.* **16** 3227
[14] Peña A, Gutiérrez J, Campo J, Barandiarán J M, Lezama L, Gil de Muro I and Rojo T 2008 *Eur. J. Inorg. Chem.* **18** 2569
[15] Ahn K H, Wu X W, Liu K and Chien C L 1996 *Phys. Rev.* B **54** 15299
[16] Righi L, Gorria P, Insausti M, Gutiérrez J and Barandiarán J M 1997 *J. Appl. Phys.* **81** 5767
Pissas M, Kallias G, Devlin E, Simopoulos A and Niarchos D 1997 *J. Appl. Phys.* **81** 5770
[17] Gutiérrez J, Barandiarán J M, Insausti M, Lezama L, Peña A, Blanco J J and Rojo T 1998 *J. Appl. Phys.* **83** 7171
[18] Ghosh K, Ogale S B, Ramesh R, Greene R L, Venkatesan T, Gapchup K M, Bathe R and Patil S I 1999 *Phys. Rev.* B **59** 533
[19] Korotin M A, Yu Ezhov S, Solovyev I V, Anisimov V I, Khomskii D I and Sawatzky G A 1996 *Phys. Rev.* B **54** 5309
[20] Ravindran P, Fjellvag H, Kjekshus A, Blaha P, Schwarz K and Luitz J 2002 *J. Appl. Phys.* **91** 291
[21] Hong C S, Kim W S and Hur N H 2001 *Phys. Rev.* B **63** 92504
[22] Jiang Wanjun, Zhou X Z, Williams Gwyn, Mukovskii Y and Glazyrin K 2007 *Phys. Rev. Lett.* **99** 177203
[23] Taran S, Chaudhuri B K, Chatterjee S, Yang H D, Neeleshwar S and Chen Y Y 2005 *J. Appl. Phys.* **98** 103903
[24] Rößler S, Rößler U K, Nenkov K, Eckert D, Yusuf S M, Dörr K and Müller K-H 2004 *Phys. Rev.* B **70** 104417
[25] Kim D, Revaz B, Zink B L, Hellman F, Rhyne J J and Mitchell J F 2002 *Phys. Rev. Lett.* **89** 227202
[26] Wei L, Kunkel H P, Zhou X Z, Williams Gwyn, Mukovskii Y and Shulyatev D 2004 *Phys. Rev.* B **70** 214413
[27] Jiang Wanjun, Zhou X Z, Williams Gwyn, Mukovskii Y and Glazyrin K 2008 *Phys. Rev.* B **77** 064424
[28] Moutis N, Panagiotopoulos I, Pissas M and Niarchos D 1999 *Phys. Rev.* B **59** 1129
[29] Assaridis H, Panagiotopoulos I, Moukarika A, Papaefthymiou V and Bakas T 2006 *Solid State Commun.* **139** 473

[30] Nair S, Banerjee A, Narlikar A V, Prabhakaran D and Boothroyd A T 2003 *Phys. Rev.* B **68** 132404
[31] Mohan Ch V, Seeger M, Kronmüller H and Murugaraj P 1998 *J. Magn. Magn. Mater.* **183** 348
[32] Kim D, Zink B L, Hellman F and Coey J M D 2002 *Phys. Rev.* B **65** 214424
[33] Ghosh K, Lobb C J, Greene R L, Karabashev S G, Shulyatev D A, Arsenov A A and Mukovskii Y 1998 *Phys. Rev. Lett.* **81** 4740
[34] Khiem N V, Phong P T, Bau L V, Nam D N H, Hong L V and Phuc N X 2009 *J. Magn. Magn. Mater.* **321** 2027
[35] Khiem N V, Bau L V, Phong P T, Hong L V, Dai N V, Nam D N H and Phuc N X 2008 *J. Korean Phys. Soc.* **52** 1518
[36] Chen L, He J H, Mei Y, Cao Y Z, Xia W W, Xu H F, Zhu Z W and Xu Z A 2009 *Physica* B **404** 1879
[37] Phan T L, Min S G, Yu S C and Oh S K 2006 *J. Magn. Magn. Mater.* **304** e778
[38] Heilman A K, Xue Y Y, Lorenz B, Gospodinov M, Dobreva S G and Chu C W 2004 *Physica* C **341–348** 707
[39] Peles A, Kunkel H P, Zhou X Z and Williams Gwyn 1999 *J. Phys.: Condens. Matter* **11** 8111
[40] Le Guillou J C and Zinn-Justin J 1980 *Phys. Rev.* B **21** 3976
[41] Kaul S N and Sambasiva Rao M 1994 *J. Phys.: Condens. Matter* **6** 7403
Kaul S N and Sambasiva Rao M 1991 *Phys. Rev. B* **43** 11240
[42] Kaul S N 1988 *Phys. Rev.* B **38** 9178
[43] Srinath S, Kaul S N and Kronmüller H 1999 *Phys. Rev.* B **59** 1145
[44] Srinath S, Kaul S N and Sostarich M-K 2000 *Phys. Rev.* B **62** 11649
[45] Kaul S N 1985 *J. Magn. Magn. Mater.* **53** 5
[46] Aharony A and Fisher M E 1973 *Phys. Rev.* B **8** 3323
[47] Bruce A D and Aharony A 1974 *Phys. Rev.* B **10** 2078
[48] Nattermann T and Trimper S 1976 *J. Phys. C: Solid State Phys.* **9** 2589
[49] Bruce A D, Kosterlitz J M and Nelson D R 1976 *J. Phys. C: Solid State Phys.* **9** 825
[50] Bruce A D 1977 *J. Phys. C: Solid State Phys.* **10** 419
[51] Frey E and Schwabl F 1991 *Phys. Rev.* B **43** 833
[52] Riedel E K and Wegner F J 1974 *Phys. Rev.* B **9** 294
[53] Kogon H S and Bruce A D 1982 *J. Phys. C: Solid State Phys.* **15** 5729
[54] Goodenough J B and Zhou J-S 2001 Localized to Itinerant Electronic Transition in Perovskite Oxides *Structure and Bonding* vol 98 ed J B Goodenough (Berlin: Springer) pp 17–114